Complement Receptor 3 Forms a Compact High-Affinity Complex with iC3b

Rasmus K. Jensen,* Goran Bajic,[†,‡,§] Mehmet Sen,[¶] Timothy A. Springer,[‖,#] Thomas Vorup-Jensen, and Gregers R. Andersen***

Complement receptor 3 (CR3, also known as Mac-1, integrin $\alpha_M\beta_2$, or CD11b/CD18) is expressed on a subset of myeloid and certain activated lymphoid cells. CR3 is essential for the phagocytosis of complement-opsonized particles such as pathogens and apoptotic or necrotic cells opsonized with the complement fragment iC3b and, to a lesser extent, C3dg. Although the interaction between the iC3b thioester domain and the ligand binding CR3 α_M I-domain is structurally and functionally well characterized, the nature of additional CR3–iC3b interactions required for phagocytosis of complement-opsonized objects remains obscure. In this study, we analyzed the interaction between iC3b and the 150-kDa headpiece fragment of the CR3 ectodomain. Surface plasmon resonance experiments demonstrated a 30 nM affinity of the CR3 headpiece for iC3b compared with 515 nM for the iC3b thioester domain, whereas experiments monitoring binding of iC3b to CR3-expressing cells suggested an affinity of 50 nM for the CR3–iC3b interaction. Small angle x-ray scattering analysis revealed that iC3b adopts an extended but preferred conformation in solution. Upon interaction with CR3, iC3b rearranges to form a compact receptor–ligand complex. Overall, the data suggest that the iC3b–CR3 interaction is of high affinity and relies on minor contacts formed between CR3 and regions outside the iC3b thioester domain. Our results rationalize the more efficient phagocytosis elicited by iC3b than by C3dg and pave the way for the development of specific therapeutics for the treatment of inflammatory and neurodegenerative diseases that do not interfere with the recognition of noncomplement CR3 ligands. ***The Journal of Immunology*, 2021, 206: 3032–3042.**

The complement system is a central part of vertebrate innate immunity. It connects to other branches of the immune system, including adaptive immunity through its functions, especially in the stimulation of Ab formation. Complement is a tightly regulated proteolytic cascade, which upon activation, leads to cleavage of the 186 kDa complement component 3 (C3) into an anaphylatoxin C3a and the opsonin C3b (Fig. 1A). C3b is deposited on the surface of the complement activator through covalent bond formation when an activator nucleophile reacts with an exposed thioester (TE) present in the TE domain of nascent C3b. Host cells present glycans that attract the fluid-phase regulator factor H and also express complement regulators membrane cofactor protein (MCP/CD46) and CR1/CD35. These regulators bind specifically to C3b and enable its degradation by the protease factor I (FI). As a result, C3b is quickly converted to iC3b (1), which acts as a powerful opsonin as it is recognized by complement receptor 2 as well as the two integrin receptors complement receptor 3 (CR3) (CD11b/CD18 or integrin $\alpha_M\beta_2$) and CR4 (p150, p95, CD11c/CD18, or integrin $\alpha_X\beta_2$). Whereas C3b has a well-defined conformation, double cleavage by FI of C3b in one of two connections to its CUB domain leads to a flexible attachment of the thioester domain to the C3c moiety (Fig. 1A) (2–4). Hydrogen deuterium exchange suggested that in iC3b, the remnants of the degraded CUB domain become surface exposed and disordered (5).

Recognition of iC3b by CR3 leads to several physiological responses dependent on the cell type and activation state of the CR3-expressing cell, including phagocytosis of dying host cells or pathogens (6, 7). CR3, consisting of the noncovalently associated integrin α_M and β_2 subunits, is highly expressed on the plasma membrane of myeloid cells, including macrophages, monocytes, dendritic cells, and neutrophil granulocytes, and is upregulated from storage granules upon stimulation. Certain lymphoid leukocytes such as NK cells and activated T cells also express CR3, and expression is further inducible in other leukocytes (6, 7). CR3 is also highly expressed in microglia, the mononuclear phagocytes of the CNS, in which CR3-mediated phagocytosis of iC3b opsonized presynaptic termini of neurons is important for neural development and homeostasis (8–11). In vivo studies leave no doubt about the importance of CR3-supported mechanisms, both as a protective agent against infection (12) and as an aggravating factor in diseases with a poorly regulated inflammatory response, for instance, as observed in animal models of multiple sclerosis and Alzheimer disease (12, 13). CR3 also plays a key role in complement stimulation of the adaptive immune system. Immune complexes containing

*Department of Molecular Biology and Genetics, Aarhus University, Aarhus, Denmark; [†]Laboratory of Molecular Medicine, Boston Children's Hospital, Harvard Medical School, Boston, MA; [‡]Department of Pediatrics, Harvard Medical School, Boston, MA; [§]Department of Microbiology, Icahn School of Medicine at Mount Sinai, New York, NY; [¶]Department of Biology and Biochemistry, University of Houston, Houston, TX; [‖]Department of Biological Chemistry and Molecular Pharmacology, Harvard Medical School, Boston, MA; [#]Program in Cellular and Molecular Medicine, Boston Children's Hospital, Boston, MA; and **Department of Biomedicine, Aarhus University, Aarhus, Denmark

ORCIDs: 0000-0001-5472-4862 (R.K.J.); 0000-0003-0480-4324 (G.B.); 0000-0002-9882-5590 (M.S.); 0000-0001-6627-2904 (T.A.S.); 0000-0001-6292-3319 (G.R.A.).

Received for publication October 26, 2020. Accepted for publication April 13, 2021.

This work was supported by the Lundbeck Foundation (BRAINSTRUC, Grant R155-2015-2666) and the Danish Agency Foundation for Science and Higher Education (Grant 4181-00137).

Address correspondence and reprint requests to Prof. Gregers R. Andersen, Department of Molecular Biology and Genetics, Aarhus University, Gustav Wieds Vej 10C, DK8000 Aarhus, Denmark. E-mail address: gra@mbg.au.dk

The online version of this article contains supplemental material.

Abbreviations used in this article: BLI, bio-layer interferometry; C3, complement component 3; CR3, complement receptor 3; EM, electron microscopy; FI, factor I; HEK, human embryonic kidney; iC3b*, Alexa Fluor 488–conjugated iC3b; MFI, mean fluorescence intensity; α_MI, α_M-chain I-domain; nsEM, negative stain EM; RCSB, Research Collaboratory for Structural Bioinformatics; SAXS, small angle x-ray scattering; SEC, size exclusion chromatography; SPR, surface plasmon resonance; TE, thioester.

complement-opsonized Ags drain with the afferent lymphatics into the subcapsular sinus where complement-opsonized Ags are taken up by subcapsular sinus macrophages via CR3 and are carried across the subcapsular sinus floor. Next, the Ag is handed off to noncognate B cells via complement receptor 2, which transports it into the follicle (14).

CR3, similar to other integrins, adopts at least three distinct conformations in the cell membrane, which control the activity of the protein. These conformations are the bent "closed" and extended closed conformations with low affinity for ligands and the extended "open" conformation with high affinity (15) (Fig. 1B). The conformation of integrins is regulated through inside-out signaling, in which stimuli received by the cell through other receptors are signaled to the integrin, and outside-in signaling, in which a ligand is recognized by the integrin. This signaling, together with the signal of tensile force relayed through the integrin, stabilizes the high-affinity conformation (16–18).

In the CR3 α_M-chain, the I-domain (α_M-chain I-domain [α_MI]) contains the primary ligand binding site, with a metal ion–dependent binding site at its center. The I-domain binds a plethora of ligands, including iC3b, ICAM-1, RAGE, platelet factor 4, mindin, platelet glycoprotein Ib, sialylated FcγRIIA, CD40L, LL-37, LRP1, fibrinogen, and the LukAB cytotoxin (19–28). Many of these interactions seem at least in part to rely on the ability of the α_MI to weakly bind glutamate side chains, which translates into avid interactions from multivalent binding of membrane-tethered CR3 (29). By contrast, C3 fragments present distinct high-affinity interactions. We previously established that the major binding site for the CR3 α_MI is located in the TE domain of iC3b, and this interaction is characterized by a K_d of 600 nM (30). However, prior studies suggested that the full-length receptor has a higher affinity for iC3b (31, 32), and other studies (33–36) proposed one or more additional recognition sites between iC3b and CR3. A recent structural analysis by negative stain electron microscopy (EM) (nsEM) of the iC3b–CR3 headpiece complex suggested the proximity of regions in iC3b close to the C345c domain and the β-propeller/β I-like domain portion of the CR3 headpiece. However, a three-dimensional reconstruction was not obtained, and the authors suggested that the tendency of the CR3 headpiece to lay flat on EM grids may have broken a three-dimensional interaction between the iC3b C345c domain and CR3 (2).

To investigate whether the iC3b–CR3 complex is an ordered complex with a specific conformation or a flexible ensemble of conformations because of iC3b flexibility, we analyzed the complex between iC3b and the CR3 headpiece in solution through multiple biochemical and biophysical techniques. We now show that the CR3–iC3b interaction is characterized by a 17-fold higher affinity than the minimal complex between the iC3b TE domain and the CR3 α_M I-domain (30). Small angle x-ray scattering (SAXS) rigid body analysis suggests that the iC3b undergoes a significant conformational change upon CR3 recognition, allowing CR3 to interact with regions outside the iC3b thioester domain.

Materials and Methods

Generation of a stable cell line expressing the CR3 headpiece fragment

The coding sequence of the human CR3 α_M-chain residues 17–773 containing the glycan knockout mutations N224R/N680R and β_2-chain residues 23–504 were cloned into the pIRES2-EGFP–based in-house vectors ET10c and ET10b, respectively. The ET10c vector contains a human rhinovirus 3C protease recognition site, an acid coiled–coil region, a StrepII-tag, and a His_6-tag on the 3′, directly in-frame with the cloning site. The open reading frame was subsequently subcloned into pcDNA3.1(+). The ET10b vector contains a human rhinovirus 3C protease recognition site, a basic coiled–coil region, and a His_6-tag directly in-frame with the cloning site. The CR3 α_M- and β_2-chain were cotransfected into human embryonic kidney (HEK) 293S GnTi$^-$ cells (American Type Culture Collection). The selection antibiotics hygromycin B and G418 at 200 μg/ml and 1 g/ml, respectively, were added to the cultures 48 h posttransfection. After selection, the cells were assessed for GFP expression using FACS, and the top 5% expressing clones were seeded in a 96-well cell culture plate. A final selection step was performed on the cell supernatants using sandwich ELISA by capturing the CR3 headpiece by use of an anti-CR3 α_M-chain Ab (CBRM 1/2) and detected using a biotinylated anti-CR3 β_2-chain Ab (IB4).

Expression and purification of CR3 headpiece

The CR3 headpiece stably transfected HEK293S cells were kept as adhesion cell culture growing in DMEM GlutaMAX (Life Technologies) supplemented with 10% (v/v) FBS, 20 mM HEPES (pH 7.5), 1% penicillin–streptomycin (Life Technologies), 200 μg/ml hygromycin B (Sigma-Aldrich), and 200 μg/ml G418 (Sigma-Aldrich). Before large-scale purification, the cells were adapted to serum-free medium. The cell supernatant was harvested by centrifugation and subsequently filtered through 0.2-μm filters. The cleared cell supernatant was supplemented with 50 mM Tris (pH 8), 500 mM NaCl, 5 mM $MgCl_2$, and 1 mM $CaCl_2$ and applied to a 5 ml HisTrap Excel (GE Healthcare). Afterwards, the column was washed with 40 ml of 20 mM Tris (pH 8), 1.5 M NaCl, 5 mM $MgCl_2$, and 1 mM $CaCl_2$, and the protein was eluted in 20 ml of 20 mM Tris (pH 8), 150 mM NaCl, 5 mM $MgCl_2$, 1 mM $CaCl_2$, and 400 mM imidazole. The elution was applied to a 1 ml Strep-Tactin column (GE Healthcare) equilibrated in 20 mM HEPES (pH 7.5), 150 mM NaCl, 5 mM $MgCl_2$, and 1 mM $CaCl_2$. The column was washed in 20 mM HEPES (pH 7.5), 150 mM NaCl, 5 mM $MgCl_2$, and 1 mM $CaCl_2$, and the protein was subsequently eluted in 20 mM HEPES (pH 7.5), 150 mM NaCl, 5 mM $MgCl_2$, 1 mM $CaCl_2$, and 2.5 mM D-desthiobiotin. 3C rhinovirus protease was added in a 1:10 mass ratio to CR3, and the reaction was allowed to proceed at 4°C overnight. A final polishing step was performed by size exclusion chromatography (SEC) on a 24 ml Superdex 200 increase (GE Healthcare) equilibrated in 20 mM HEPES (pH 7.5), 150 mM NaCl, 5 mM $MgCl_2$, and 1 mM $CaCl_2$.

Single-particle nsEM

Carbon-evaporated copper grids (G400-C3, Gilder) were glow discharged for 45 s at 25 mA using an easiGlow (PELCO). Then, 3 μl of CR3 headpiece at 13 μg/ml was adsorbed to the grid for 5 s before being blotted away. The grid was washed twice in 3 μl of 20 mM HEPES (pH 7.5) and 150 mM NaCl, followed by a staining step using a 3-μl drop of 2% (w/v) uranyl formate, allowing it to stain the grid for 45 s. The grids were imaged on a 120 kV Tecnai G2 spirit. Automated data collection was performed at a nominal magnification of 67.000× and a defocus ranging from −0.7 to −1.7 μm using Leginon (37). Particles were picked using DoG picker (38) in the Appion framework (39). Two-dimensional classification, initial model generation using stochastic gradient descent and three-dimensional classification was performed in RELION (40).

Surface plasmon resonance assays

Recombinant human C3d containing the native Cys^{1010} was prepared as described for C3d C1010A (30), except that all buffers contained 5 mM β-mercaptoethanol. Immediately prior to biotinylation, the β-mercaptoethanol was removed by buffer exchange into 20 mM HEPES (pH 7.0) and 150 mM NaCl using a PD10 desalting column (GE Healthcare). EZ-Link Maleimide-PEG2-Biotin (Thermo Fisher Scientific) was added to C3d in 5-fold molar excess and incubated at 4°C for 6 h. The reaction was quenched by the addition of 100 mM Tris (pH 8.5), and the biotinylated C3d was applied to a 24 ml Superdex 75 (GE Healthcare) equilibrated in 20 mM HEPES (pH 7.5) and 150 mM NaCl. Biotinylated C3, C3b, and iC3b was generated and purified (as described in Refs. 41 and 42). The experiments were performed on a Biacore T200 instrument with a running buffer containing 20 mM HEPES (pH 7.5), 150 mM NaCl, 5 mM $MgCl_2$, and 1 mM $CaCl_2$, unless otherwise stated. Streptavidin was immobilized on a CMD500M chip (XanTec Bioanalytics) to 200 response units. C3d or iC3b biotinylated on the thioester cysteine was injected on the chip until the surface was saturated. For the kinetics experiments using iC3b, the CR3 headpiece was injected in a concentration series ranging from 0.3215 nM to 100 nM, whereas for C3d, the CR3 headpiece was injected in a concentration series ranging from 3.25 nM to 2000 nM. The surface was regenerated by using a buffer containing 50 mM EDTA, 1 M NaCl, and 100 mM HEPES (pH 7.5). The data were analyzed using a 1:1 binding model, and the reported on- and off-rates are averages of three independent experiments. The kinetic experiment with iC3b on the surface was repeated three times in the buffer containing 20 mM HEPES (pH 7.5), 150 mM NaCl, 1 mM $MnCl_2$, and 0.2 mM $CaCl_2$ as well. The competition assays were

performed on the iC3b surface where 20 nM of CR3 headpiece was injected either alone or preincubated on ice for 1 h with 10, 20, 50, 100, 200, or 1000 nM of iC3b, C3d, or C3b, respectively. All experiments were performed in triplicates.

Bio-layer interferometry

The bio-layer interferometry (BLI) experiment were performed on an Octet RED96 (ForteBio) at 30°C and shaking at 1000 rpm. The running and wash buffer contained 20 mM HEPES (pH 7.5), 150 mM NaCl, 1 mM $CaCl_2$, and 1 mg/ml BSA. Biotinylated iC3b was loaded on streptavidin sensors (ForteBio) for 10 min at 5 μg/ml, in which the sensors were washed for 2 min in running buffer. The association of iC3b to CR3 headpiece (1000, 500, 250, 125, 62.5, and 31.3 nM) was measured for 150 s, followed by a 200 s dissociation period. The association was modeled as $R(t) = R_{max}([CR3]/([CR3] + K_d)(1 - \exp(-t(k_{on}[CR3] - k_{off})))$, $K_d = k_{on}/k_{off}$, and the dissociation was modeled as a first-order exponential decay, $R(t) = R(150)\exp(-k_{off}(t - 150\ s))$.

Analytical SEC analysis

For analyzing the effect of different divalent cations on the oligomeric state of CR3, 50 μl of CR3 headpiece at 2 μg/μl was diluted 4-fold in either 20 mM HEPES (pH 7.5), 150 mM NaCl, 1 mM $MnCl_2$, and 0.2 mM $CaCl_2$; 20 mM HEPES (pH 7.5), 150 mM NaCl, 5 mM $MgCl_2$, and 1 mM $CaCl_2$; or 20 mM HEPES (pH 7.5), 150 mM NaCl, 5 mM $NiCl_2$, and 1 mM $CaCl_2$. The protein was incubated for 1 h at room temperature before being injected on a 24 ml Superdex 200 increase equilibrated in the respective protein dilution buffer. For analyzing the complex formation between CR3 and iC3b, 15 μg of iC3b was mixed with 1.1-fold molar excess of CR3. The sample was injected on a 2.4 ml Superdex 200 increase equilibrated in 20 mM HEPES (pH 7.5), 150 mM NaCl, 5 mM $MgCl_2$, and 1 mM $CaCl_2$. Control experiments injecting either CR3 or iC3b in the same amount was also performed.

iC3b affinity for cell-bound CR3 and competition with the CR3 headpiece

C3b at 2.2 mg/ml in 20 mM HEPES (pH 7.5) and 150 mM NaCl was added to 20 mM sodium bicarbonate (pH 9.0), yielding a final pH of ∼8.3. A 5-fold molar excess of Alexa Fluor 488 NHS Ester (Molecular Probes) was added to the C3b solution. The reaction was incubated for 1 h at room temperature and protected from light. The reaction was quenched by the addition of 100 mM Tris (pH 8.5), and unreacted dye was removed by SEC using a 24 ml Superdex 200 increase (GE Healthcare) equilibrated in 20 mM HEPES (pH 7.5) and 150 mM NaCl. The resulting Alexa Fluor 488–conjugated C3b was cleaved into iC3b and purified as described for regular iC3b, except that at all steps, the protein was protected from light. Equilibrium binding by iC3b to CR3 expressed in the cell membrane was carried out with a protocol and experimental data analysis modified from (43). K562 cells with recombinant expression of CR3 (CR3/K562) and the parental wild-type K562 cell were cultured as described (44). The cells were washed and adjusted to a concentration of 5×10^6 cells/ml in sterile-filtered 5 mM D-glucose, 5 mg/ml human serum albumin (CSL Behring), 150 mM NaCl, 5 mM KCl, 1 mM $MgCl_2$, 1.8 mM $CaCl_2$, and 10 mM HEPES (pH 7.4) (binding buffer). Wells in a flow cytometry microtiter plate each received 100 μl of cell suspension. For integrin activation, wells also received $MnCl_2$ to a final concentration of 1 mM or KIM127 mAb (45) to a final concentration of 5 μg/ml. Finally, Alexa Fluor 488–conjugated iC3b (iC3b*) was titrated in concentrations of 16, 23, 35, 53, 80, and 120 nM in either conditions with Mn^{2+} or KIM127. As controls, K562 cells not expressing CR3 with integrin activating agents and 21 μg/ml iC3b* were prepared. Cells were incubated at room temperature for 45 min. This incubation time was chosen (as outlined in Ref. 46), taking into account the surface plasmon resonance (SPR)–determined off-rates in this study at 3.6×10^{-2} s^{-1} in the presence of Mg^{2+} for experiments with KIM127 corresponding to a time to reach equilibrium at $5 \times (\ln 2/36 \times 10^{-3}\ s^{-1})$, that is 1.6 min or 48 min for experiments with Mn^{2+} with the off-rate at 1.2×10^{-3} s^{-1}. A volume of 100 μl binding buffer with integrin activating agents was added to wells, and the cells were pelleted by centrifugation at 400 × *g* for 3 min. The plate was emptied, and cells were resuspended in PBS (pH 7.4) with 0.99% (v/v) formaldehyde to covalently fix bound iC3b* on the cell surface. The fluorescence signals were recorded in a NovoCyte flow cytometer (Agilent Technologies) and analyzed as mean fluorescent intensities (MFI) in the FlowJo software (BD Life Sciences). Events were gated in a forward–side scatter diagram to exclude debris, followed by quantification of the MFI. The CR3-specific signal (ΔMFI) was calculated by subtracting the signal for K562 cells in the presence of activating agent and 120 nm iC3b* from the signal for CR3/K562. The experimental data were fitted to a 1:1 Langmuir–Hill binding isotherm:

$$\Delta MFI = \frac{\Delta MFI_{Max}}{1 + \left(\frac{K_{d,App}}{c_{iC3b*}}\right)^{n_{Hill}}}, \quad (1)$$

where $K_{d,\ App}$ is the apparent equilibrium dissociation constant, n_{Hill} the Hill coefficient, c_{iC3b*} the concentration of iC3b*, and ΔMFI_{Max} the ΔMFI at binding saturation.

For analysis of the competition between cell membrane–expressed CR3 and soluble CR3 headpiece, the protocol described above was modified by fixing the concentration of iC3b* to 80 nM and titrating the concentration of CR3 headpiece in concentrations of 9, 21, 45, 69, 104, and 156 nM. The ΔMFI levels were normalized to the response in the absence of the CR3 headpiece (ΔMFI_0). Experimental data were fitted with a model derived from Eq. 1:

$$100\% \cdot \frac{\Delta MFI}{\Delta MFI_0} = \frac{100\%}{1 + \left(\frac{IC_{50}}{c_{CR3hp}}\right)^{n_{Hill}}}. \quad (2)$$

All statistical calculations and curve fitting for the experiments involving K562 cells was made in GraphPad Prism (ver. 9.0.2).

SAXS data collection and analysis

In-line SEC–SAXS data for the CR3 headpiece in complex with iC3b were collected at the P12 beamline at PETRA III (Hamburg, Germany) (47). Scattering was recorded from the elution of a 24 ml Superdex 200 increase equilibrated in 20 mM HEPES (pH 7.5), 150 mM NaCl, 5 mM $MgCl_2$, and 1 mM $CaCl_2$ with a flow rate of 0.25 ml/min. The CR3 headpiece was mixed with 1.2-fold molar excess of iC3b and subsequently injected on the SEC column. Each frame during the SEC–SAXS run covers a 0.955-s exposure performed every second. The sample-to-detector distance was 3.0 m covering $0.02 < q < 4.8\ nm^{-1}$ ($q = 4\pi \cdot \sin\theta \cdot \lambda^{-1}$, where 2θ is the scattering angle). Normalization and radial averaging was performed at the beamline using the automated pipeline (47, 48). Buffer subtraction was performed using CHROMIXS (49). Because of the high level of averaging performed during SEC–SAXS data processing, detector imperfections most likely led to the error estimates being underestimated at low q, as revealed an indirect Fourier transform of the data. The error estimates were therefore rescaled by $Err = Err_{original}(1 + 2.5 \cdot \times \exp(-7q^2))$. Forty ab initio models were generated using dammif in slow mode, and the resulting models were clustered using damclust (50). This led to six clusters with only one major cluster containing 32 of the 40 models. The models of each cluster was subsequently averaged and filtered, yielding the final models of each cluster. SAXS measurements of CR3 headpiece, C3b, and iC3b in batch mode were likewise collected at the P12 beamline. The data were collected in a temperature-controlled capillary at 20°C using a PILATUS 2M pixel detector (DECTRIS) with λ = 1.240 Å. The sample-to-detector distance was 3.0 m covering $0.02 < q < 4.8\ nm^{-1}$. Samples of CR3 were prepared at 0.7, 1.3, 1.7, and 2.9 mg/ml, and samples of C3b and iC3b were prepared at 7.3 and 13.0 mg/ml, respectively. Data were collected with twenty exposures of 45 ms. Radial averaging, buffer subtraction, and concentration scaling was performed by the automated beamline pipeline (51), and the pair distribution function was calculated by indirect Fourier transformation using GNOM (52).

SAXS rigid body modeling

Rigid body modeling using CORAL (50) was performed for C3b, iC3b, and the CR3:iC3b complex against their corresponding SAXS curves. Input domains for C3b and iC3b was extracted from Research Collaboratory for Structural Bioinformatics (RCSB) entry 6EHG (41) after aligning the principal inertial vectors of the structure with the Cartesian axes using alpraxin (53). For C3b, the MG1-6, MG7, C345c, and the CUB-TE fragment were extracted as separate entities. The rigid bodies were connected using LINK statements to model the missing linker regions. The MG1–7 and MG8 rigid bodies were fixed relative to each other such that the MG-ring was kept intact, and a distance restraint of 6 Å was applied between Cys^{873} in the MG8 domain and Cys^{1513} in the C345c domain to maintain their disulphide bridge. Twenty rigid body models were generated with CORAL, which are all shown in Supplemental Fig. 3E. For iC3b, a similar scheme was used, except that the CUB domain was modeled using dummy residues to represent all three flexible stretches of the degraded domain. This was done by 1) introducing a LINK statement connecting the MG7 C-terminal residue to the N-terminal residue of the TE domain, 2) introducing a CTER statement at the C-terminal residue of the TE domain, or 3) introducing a NTER statement at the N-terminal residue of the MG8 domain. One hundred CORAL runs were performed, half using an input model in which the TE domain was placed in a C3b-like conformation and the other half in which the TE domain was placed beside the C345c domain. No systematic differences could be observed between the models coming from either input models. For

the CR3:iC3b complex, iC3b was modeled as for free iC3b, except that the TE domain was fixed relative to the α_MI of CR3 to keep the interface known from the crystal structure of the complex [RCSB entry 4M76 (30)] intact. The N- and C-terminal residues of the CR3 α_MI were restrained with two distance restraints of either 7 or 9 Å to the α_M β-propeller because with distance restraints of 5 Å, very few models obtained $\chi^2 < 3$. The rest of the CR3 headpiece was kept as a single rigid body using a homology model based on $\alpha_X\beta_2$ (RCSB entry 4NEH), modeled in the open conformation using the β-chain from the crystal structure of $\alpha_{IIb}\beta_3$ [RCSB entry 2VDR (54)]. Three consecutive rounds of rigid body modeling were performed in rounds 2 and 3, starting from the best fitting model of the prior round. To sample the rigid body movement more finely, the CORAL parameters "angular step" and "spatial step" were decreased from the default 20° and 5 Å to 10° and 2.5 Å, respectively, during optimization. No systematic differences could be observed between the models coming from different input models and subject to 7- or 9-Å distance restraints. Hence, a total of 135 output models were analyzed, and the best 15 models having $1.8 < \chi^2 < 2.2$ were finally clustered.

Results

The CR3 headpiece forms a high-affinity complex with iC3b

The CR3 headpiece was purified from HEK293S GnTI$^-$ cells stably transfected with plasmids encoding the α_M- and β_2-chains of the 150-kDa CR3 headpiece fragment (dashed outline, Fig. 1B). In accordance with many prior studies of integrin ectodomains, the two subunits remained firmly associated throughout all steps for expression, purification, and structural analysis. We investigated the oligomerization state of our CR3 headpiece using analytical SEC in Mn^{2+}-, Mg^{2+}-, and Ni^{2+}-containing buffers (Supplemental Fig. 1A). At low concentrations, the CR3 headpiece in both Mg^{2+} and Ni^{2+} mainly eluted as a monomer, but a small dimer fraction was also present. Conversely, in Mn^{2+}, CR3 eluted as a dimer, in agreement with prior findings that the CR3 headpiece is prone to dimerization in a divalent metal ion–dependent fashion in which the PSI/EGF domains in the β_2-subunit interact in a ligand-like fashion with the α_M I-domain (2). Concentration-dependent dimerization was further confirmed by SAXS (Supplemental Fig. 1B–E).

We further investigated the homogeneity of the CR3 headpiece using nsEM single-particle analysis. A majority of the molecules were monomers on the EM grid. Single-particle two-dimensional class averages confirmed that the majority of the CR3 headpiece molecules were monomers (Supplemental Fig. 1F), whereas a minor fraction formed dimers (Supplemental Fig. 1G). In accordance with an earlier study (2), the two-dimensional class averages containing such dimers suggested a head-to-tail organization in which the α_MI of one CR3 headpiece is interacting with the distal end of the β-leg encompassing the I-EGF1 or PSI domains of the second CR3 headpiece. In our two-dimensional class averages of the CR3 headpiece monomer, both the classical open and closed conformations of integrin headpieces were observed. This was further verified by three-dimensional classification, in which the dataset separated clearly into an open conformation expected to have high ligand affinity and a closed conformation likely to have low ligand affinity, with ∼50% of the particles in each reconstruction (Supplemental Fig. 1H, 1I).

To verify that the recombinant CR3 headpiece is able to form a stable complex with iC3b, we assessed the stability of the complex by SEC. The CR3:iC3b complex eluted earlier than either of the two individual proteins in a monodisperse peak (Fig. 1C). Next, we used SPR to measure the affinity and the kinetics of the CR3 headpiece–iC3b interaction. We coupled C3b to biotin through its free thioester cysteine side chain and subsequently converted C3b to iC3b by FI cleavage in the presence of factor H, as previously described (42). The biotinylated iC3b was then bound to a streptavidin-coated SPR chip surface. The CR3 headpiece bound iC3b in a Mg^{2+}-containing buffer with a dissociation constant K_d = 30 nM when fitted to a 1:1 interaction model (Fig. 1D, 1F, Supplemental Table I). In a Mn^{2+}-containing buffer, CR3 bound to iC3b with a significantly lower k_{on} (Fig. 1E). The dissociation rate was however 30-fold lower than with Mg^{2+}, and the CR3 affinity for iC3b in the

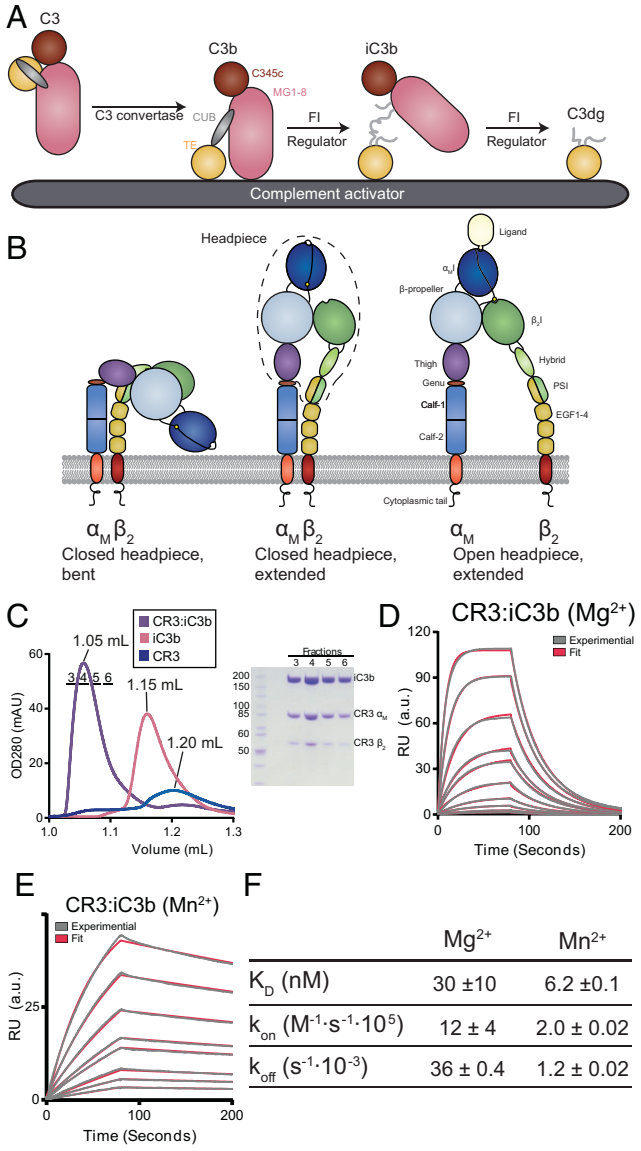

	Mg^{2+}	Mn^{2+}
K_D (nM)	30 ±10	6.2 ±0.1
k_{on} ($M^{-1}\cdot s^{-1}\cdot 10^5$)	12 ± 4	2.0 ± 0.02
k_{off} ($s^{-1}\cdot 10^{-3}$)	36 ± 0.4	1.2 ± 0.02

FIGURE 1. Characterization of the CR3 headpiece fragment. (**A**) C3 is cleaved by a C3 convertase into the opsonin C3b, which is deposited on the activator surface. C3b can then be further degraded into iC3b by the FI protease, aided by a regulator binding to C3b. FI may further degrade iC3b into C3dg. (**B**) CR3 adopts three different overall conformations. The bent conformation (left) and intermediate, extended closed conformation (middle) are low affinity. The extended, open conformation is ∼1000-fold higher affinity (right). The dashed line indicates the headpiece fragment. (**C**) SEC analysis of the complex formation between CR3 and iC3b. The complex elutes significantly earlier compared with both iC3b and CR3 alone. To the right, fractions indicated in the chromatogram by horizontal lines are analyzed by nonreducing SDS-PAGE. (**D**) SPR sensorgrams for the interaction of CR3, injected on an iC3b surface in a Mg^{2+} buffer. CR3 was injected at 100, 50, 25, 12.5, 10, 5, 2.5, 1.25, 0.63, and 0.31 nM. The raw curves are shown in gray, and the fit is shown in red. The dissociation constant calculated as $K_d = k_{off}/k_{on}$ is indicated. The on- and off-rates are the average of three independent experiments. (**E**) As in panel (D), but in a Mn^{2+} buffer, only curves for CR3 concentrations 25, 12.5, 10, 5, 2.5, 1.25, 0.63, and 0.31 nM are displayed. (**F**) Table summarizing the kinetic constants determined by SPR ± SD of three independent experiments.

presence of Mn^{2+} was therefore ~5-fold higher with an apparent dissociation constant K_d of 6.2 nM (Fig. 1E, 1F, Supplemental Table I). To measure the Mg^{2+}-independent binding of iC3b to the CR3 headpiece in the presence of Ca^{2+} only, we immobilized biotinylated iC3b to BLI sensors. We fitted the experimental curves from a set of increasing iC3b concentration to a dissociation constant K_d = 5.5 μM, whereas we obtained K_d = 22 nM in the presence of 5 mM Mg^{2+} with BLI (Supplemental Fig. 2)

Additional iC3b binding sites are present in CR3

The dissociation constant for the iC3b–CR3 headpiece complex was ~20 fold higher compared with the dissociation constant for the complex of iC3b and the CR3 α_MI (30) (Supplemental Table I). We therefore investigated whether this was due to stronger binding through the α_MI in the context of the CR3 headpiece or whether CR3 contains one or more additional interaction sites for iC3b outside of the α_MI that could explain the observed weak Mg^{2+}-independent interaction. For this purpose, we used the recombinant C3d fragment contained within C3dg but with the flexible remnants of the C3g fragment removed (30). As above, the apparent affinity of the CR3–C3d complex was measured using SPR (Fig. 2A, 2B). Because the binding kinetics were very fast and data could not be robustly fitted to a 1:1 interaction model, we instead performed a steady-state analysis and measured an apparent K_d = 515 nM similar to the 600 nM affinity of the α_MI for iC3b measured by isothermal titration calorimetry (30). This suggests that embedding of the α_MI into the CR3 headpiece does not significantly change its affinity for the C3d moiety in iC3b. Next, we performed an SPR-based competition assay in which we measured the binding of the CR3 headpiece to immobilized iC3b in the presence of increasing concentrations of free C3b, iC3b, and C3d (Fig. 2C–E). Fluid-phase iC3b and C3d competed for binding to the immobilized iC3b, whereas C3b did not, demonstrating that the competition was ligand specific. Fluid-phase iC3b robustly competed for CR3 binding, whereas by contrast, the presence of C3d only produced a marginal decrease in the binding signal, even at a 50-fold molar excess of C3d. In summary, our SPR and BLI data demonstrated that additional contacts, outside of the α_MI:TE interface described by x-ray crystallography (30), contribute to the CR3 interaction with iC3b.

Quantitative comparison of cell membrane–expressed CR3 and the CR3 headpiece

To compare the binding of iC3b to full-length CR3 expressed in the cell membrane with iC3b binding to the CR3 headpiece, we modified a previously described protocol (43) employing flow cytometry. Cell-bound CR3 was activated by the presence of either 1 mM Mn^{2+} or the mAb KIM127 at a concentration of 5 μg/ml. The K562 cells expressing CR3 were incubated with fluorophore-labeled iC3b (iC3b*) at room temperature to prevent internalization and for 45 min to reach binding equilibrium. Titration of iC3b* resulted in a highly reproducible binding to both KIM127 and Mn^{2+}-activated CR3 on K562 cells. The experimental data narrowly fitted (R^2 = 0.85 and R^2 = 0.84, respectively) a Langmuir–Hill binding isotherm with an apparent K_d at 50 nM for both approaches to CR3 activation (Fig. 3A–D). These results are in good agreement with our SPR experiments in which the CR3 headpiece bound to immobilized iC3b with K_d values of 6–30 nM iC3b (Fig. 1F). The Hill coefficient for both KIM127 and Mn^{2+}-mediated CR3 activation were fitted to values of 1.7 and 2.5, respectively, suggesting a level of positive cooperativity in the binding of iC3b* to cell-bound CR3.

Next, we asked whether our soluble CR3 headpiece could compete with cell-bound CR3. Even modest concentrations of the CR3 headpiece produced a reproducible reduction of iC3b* binding to the membrane-expressed CR3 (Fig. 3E, 3F). Compared with the binding of soluble iC3b* to cell-bound CR3, curve fitting for these competition experiments was less robust (R^2 = 0.65 and R^2 = 0.48 in the presence of KIM127 or Mn^{2+}, respectively), also reflected in the broad confidence intervals for the IC_{50} with mean values of 245 nM and 202 nM (Fig. 3E, 3F). Nevertheless, the two different means of activating CR3 gave similar IC50 values, and these values differed 4–5-fold from the apparent K_d for the simpler binding experiments shown in Fig. 3C, 3D. Overall, our SPR- and cell-based

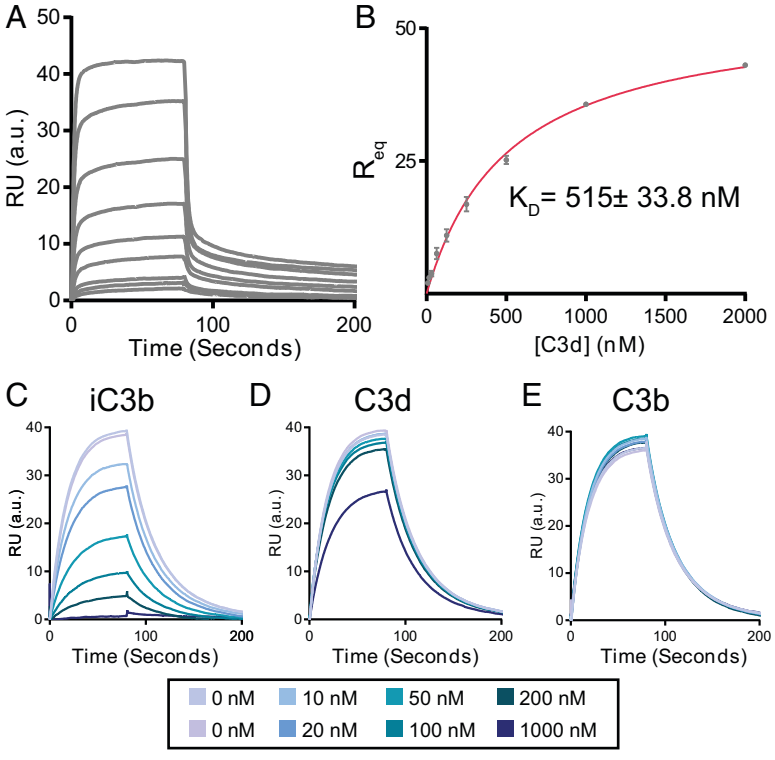

FIGURE 2. Analysis of the interaction between C3d and CR3. (**A**) A representative series of raw sensorgrams from an SPR experiment used for steady-state analysis. The CR3 headpiece at 2000, 1000, 500, 250, 125, 62.5, 31.3, 15.6, and 7.8 nM was injected on a C3d-coated sensor in a Mg^{2+} buffer. (**B**) Steady-state analysis of SPR experiments in (A). Average values ± SD for three repetitions are plotted, and the K_d value is determined by nonlinear regression and given ± SD. The resulting K_d value is 17-fold higher than the K_d determined for the CR3:iC3b complex. (**C–E**) Sensorgrams of SPR competition assays in which 20 nM of CR3 was incubated with variable concentrations of iC3b (C), C3d (D), or C3b (E) before being injected on an iC3b-coated sensor.

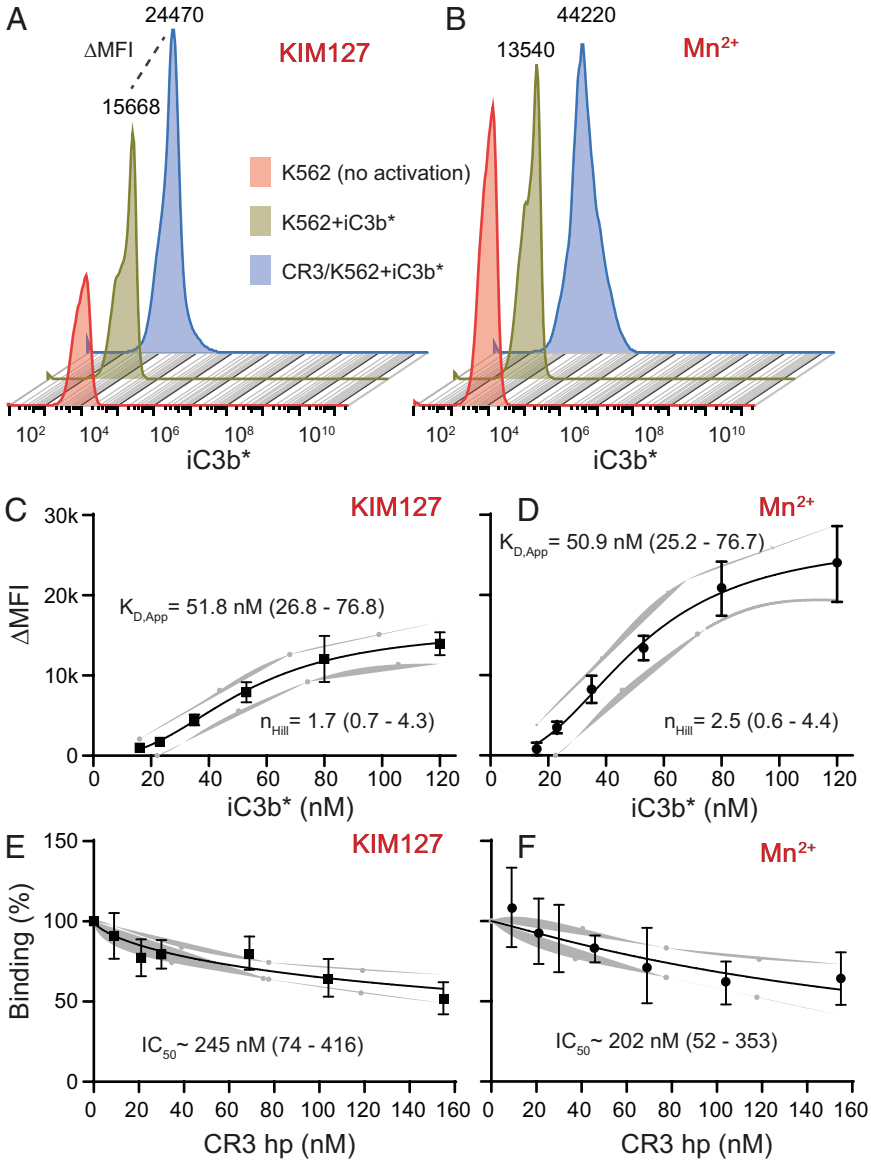

FIGURE 3. The affinity of CR3 expressed in cell surfaces for iC3b and competition with CR3 headpiece. (**A** and **B**). Histograms showing fluorescence intensity of CR3-expressing K562 cells incubated with iC3b* and activating with with KIM127 (A) or Mn^{2+} (B). Peaks are labeled with the MFI used for calculating Δ*MFI*. For reference, the autofluorescence of wild-type K562 cells is indicated. (**C** and **D**) Affinity of cell membrane–expressed CR3 for iC3. The recorded Δ*MFI* were plotted as a function of iC3b* concentration and fitted with Eq. 1. For each titration point, the mean value and SEM (error bars) are shown for three independent experiments. The 95% confidence interval of the fitting to experimental data are indicated with gray shadows. Experiments were made either with KIM127 (C) or Mn^{2+} (D) as CR3-activating agents. The calculated $K_{d,App}$ and n_{Hill} are indicated together with the confidence interval. (**E** and **F**) Competition between cell membrane–expressed CR3 and CR3hp for iC3b binding. For each titration point, the mean value and SEM are shown for three independent experiments. Experimental data, made either with KIM127 (E) or Mn^{2+} (F) as integrin-activating agents, were fitted with Eq. 2, and the IC_{50} listed together with the confidence interval. The confidence interval of the fitting is indicated with gray shadows.

interaction experiments provided solid evidence that the recombinant and soluble CR3 headpiece exhibits an affinity for the iC3b that is similar to that of the full cell-bound receptor and is affected in a similar manner by the presence of Mg^{2+}, Ca^{2+}, and Mn^{2+} cations.

iC3b adopts an extended but stable conformation

After C3b is cleaved by FI to form iC3b, the CUB domain is thought to become disordered, and the TE domain no longer closely associates with the MG-ring (2–5). To understand the structural state of the CUB and TE domains after iC3b formation, we recorded SAXS data on iC3b and, for comparison, C3b (Supplemental Fig. 3A). Guinier analysis did not suggest interparticle effects. C3b and iC3b exhibited R_g values of 49 Å and 53 Å, respectively (Supplemental Fig. 3B, 3C), well in line with earlier reports (3, 55). Comparison of the Kratky plots (Supplemental Fig. 3A) showed that iC3b adopts a more extended structure than C3b. To investigate the solution conformation of iC3b further, we performed rigid body modeling against the scattering data of iC3b. We also performed the same analysis against the data for C3b as a control (Supplemental Fig. 3D–F). The C3c fragment, excluding the C345c domain, was modeled as a single rigid body. The C345c domain was modeled independently because of the known flexibility of the domain but was restrained to maintain the disulphide to the MG7 domain. For C3b, the CUB and TE domains were treated as a single body, whereas for iC3b, the TE domain was modeled as a rigid body and the cleaved CUB domain was modeled as connected dummy residues. For C3b, all output models clustered closely, showing a slight detachment of the TE domain from the MG1 domain (Supplemental Fig. 3E, 3F), consistent with prior results (55). For iC3b, 100 independent rigid body models were generated with two different initial positions of the TE domain. In one initial model, the TE domain was positioned as in C3b, whereas in the second, the TE domain was positioned next to the C345c domain. Independent of the initial position of the TE domain, the 10 models with the best fit to the experimental data clustered closely in terms of conformation (Fig. 4A, 4C). In these models, the cleaved CUB domain adopts an extended conformation with the TE domain, and compared with C3b, it is positioned far from MG1 and the rest of the MG-ring (Fig. 4A, 4B). Apart from being detached from the MG-ring, the CUB-TE moiety has also rotated so that the TE domain is located toward the MG4 domain edge of C3c (Fig. 4A), whereas in crystal structures of C3b, the TE domain forms contacts with the MG1

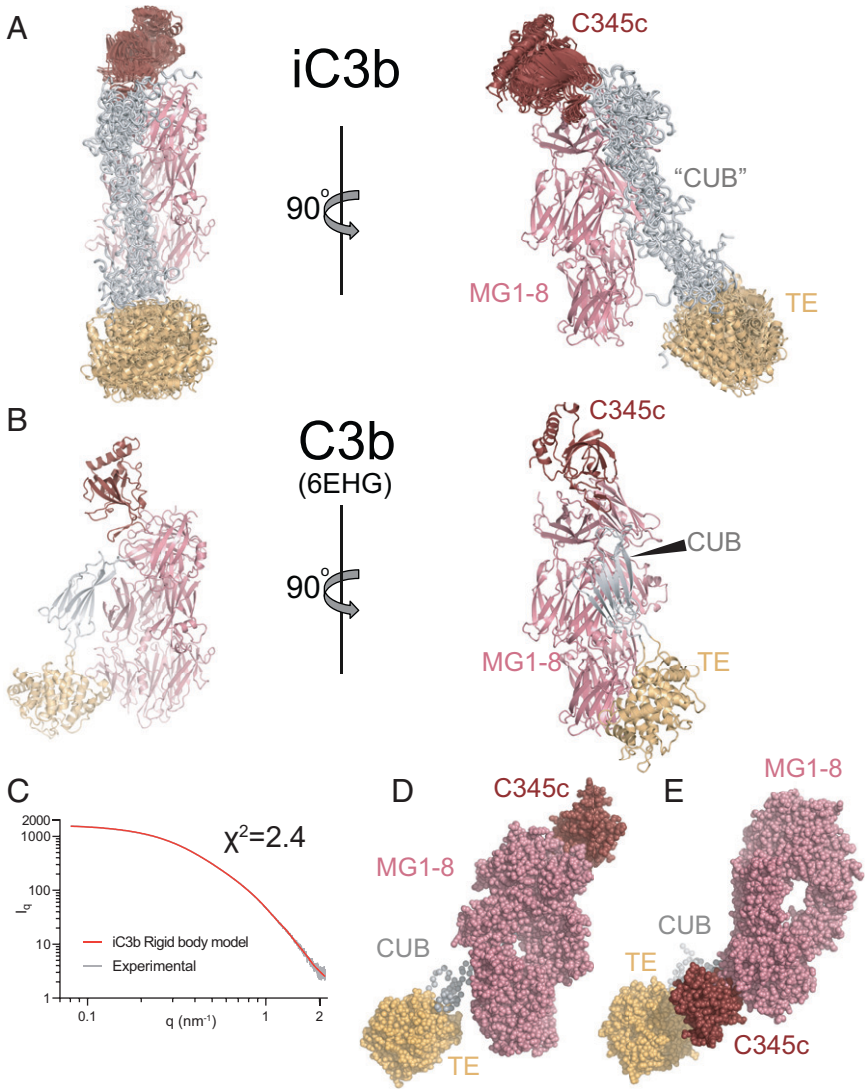

FIGURE 4. SAXS rigid body analysis of iC3b. (**A**) The 10 rigid body models with the lowest χ^2-value aligned on the MG1–6 domains. The models cluster closely together with their thioester domain displaced from the MG-ring, connected by an extended degraded CUB domain. C3b is presented in the same orientation for comparison. (**B**) Crystal structure of C3b in the two orientations used in (A) for comparison. (**C**) Comparison of the experimental scattering curve and a selected model obtained by rigid body modeling (**D**) The iC3b model with the lowest χ^2-value shown in a spheres representation. (**E**) An alternative iC3b rigid body model in which the thioester domain is in close proximity to the C345c domain. Notice how the mass distribution resembles that of the best fitting model in (C).

domain. In contrast, other models with a significantly worse fit to the data had the TE domain close to the C345c domain. A comparison of these two classes of rigid body models reveals that even though they are very different with respect to the location of the TE domain, their mass distribution is similar (Fig. 4D, 4E). In summary, the degraded CUB domain adopts an extended conformation, leading to the TE domain detaching significantly from the MG core to a preferred position rather than being randomly located relative to the C3c moiety.

The iC3b–CR3 complex is compact

To characterize the solution structure of the iC3b:CR3 headpiece complex, we collected synchrotron in-line SEC–SAXS data. The forward scattering elution profile displayed two peaks: the first one corresponding to the complex and the second one corresponding to excess iC3b (Fig. 5A, 5B). The R_g was stable throughout the first peak, demonstrating that the CR3 remained saturated with iC3b during the SEC run in agreement with the 30 nM K_d observed by SPR. A Guinier analysis of the scattering curve did not indicate interparticle effects and suggested an R_g of 67 Å for the CR3–iC3b complex (Supplemental Fig. 4A). Based on calculation of the pair distribution function, the D_{max} for the complex was ~260 Å (Supplemental Fig. 4C). In support of a well-defined and compact CR3:iC3b complex, this is only slightly larger than the ~200 Å we observe for the iC3b and the CR3 headpiece monomers.

To obtain models of the iC3b:CR3 complex and to identify the parts of iC3b involved in the complex with CR3 apart from the TE domain, we performed rigid body refinement against the SAXS data. Within the complex, iC3b was modeled as for free iC3b, except that the TE domain was fixed relative to the α_MI of CR3, to maintain the interaction known from the crystal structure. The resulting rigid body was connected through two distance restraints between the α_MI and the α_M β-propeller. This allows the α_MI to rotate relative to the rest of the CR3 headpiece. The remaining fragment of the CR3 headpiece was modeled as a single rigid body in the open conformation. To improve the model fit to the data, the position of the C3c fragment in the best initial solutions was used as a new initial model, and the translation and rotation of the rigid bodies were sampled more finely. After two iterations, this strategy converged and resulted in the best model fitting the data with $\chi^2 = 1.8$ (Fig. 5C). The 15 best fitting models with $1.8 < \chi^2 < 2.2$ were classified into three tight clusters (Fig. 5D–F, Supplemental Fig. 4D–F). In all the analyzed models, iC3b adopts a conformation markedly different from that of unbound iC3b. Relocation of the C3c moiety brings the iC3b TE domain close to the MG-ring (Fig. 5D–F) as opposed to unbound iC3b in which the TE domain is located distantly from the MG-ring (Fig. 4A). However, our models do not

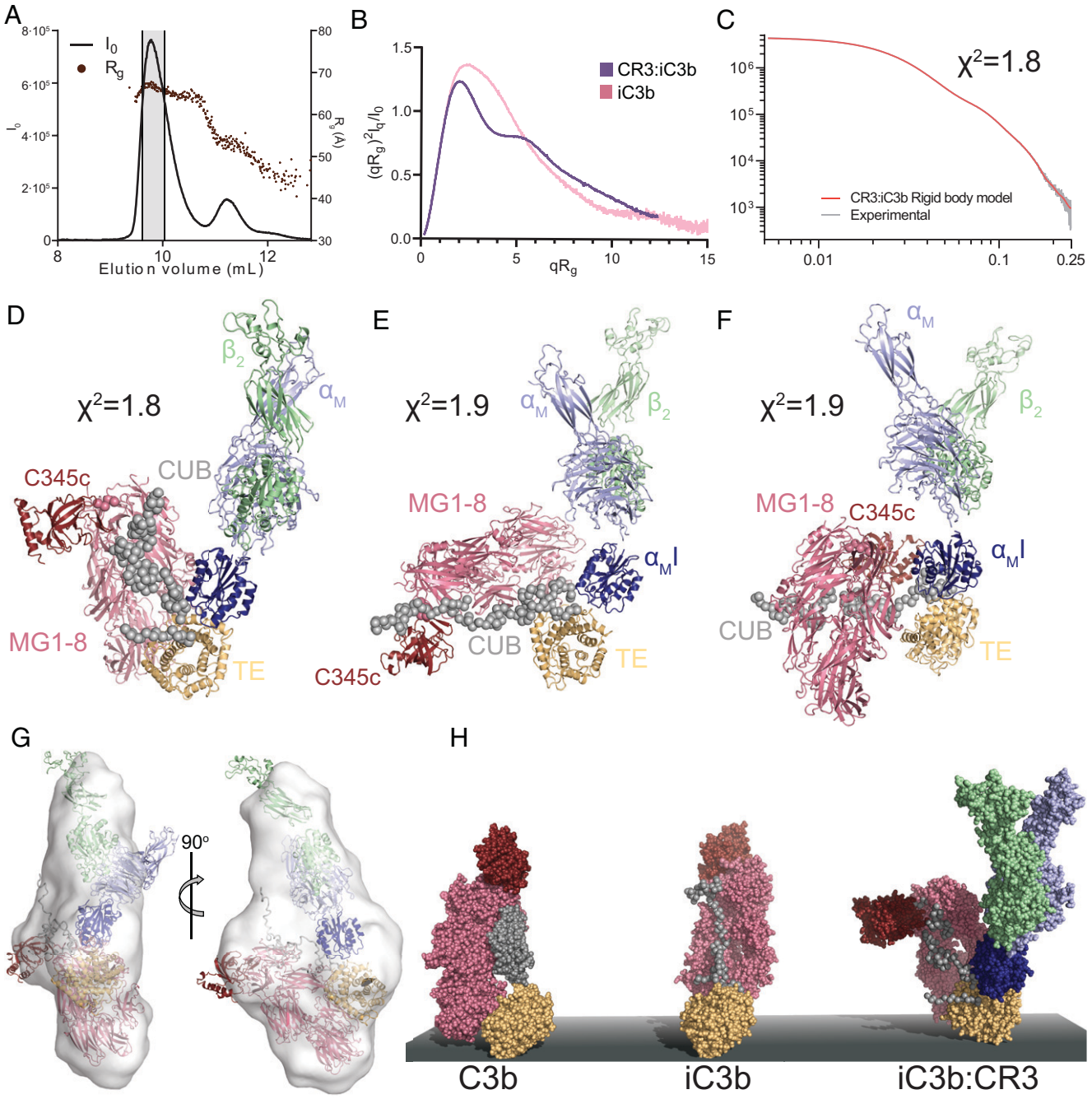

FIGURE 5. SEC–SAXS analysis of the iC3b:CR3 in complex. (**A**) The forward scattering and R_g of each frame during the SEC–SAXS experiment of the CR3:iC3b complex plotted as a function of the elution volume. The two peaks contain the CR3:iC3b complex and excess free iC3b, respectively. The experimental scattering curve for the CR3:iC3b complex was obtained from the shaded area. (**B**) The Guiner-normalized Kratky plot of the CR3:iC3b complex (purple) and iC3b alone (pink). (**C**) Experimental scattering curve (gray) compared with the curve calculated (red) from the CR3:iC3b rigid model shown in (**D**). (D–**F**) Representative rigid body models of the three clusters of rigid body models. Upon CR3 recognition, the CUB remnants reorganize, leading to a more compact iC3b conformation, but the exact position of C3c varies significantly between the three clusters. (**G**) Average model of 32 ab initio models calculated from the CR3:iC3b SEC–SAXS data aligned to the rigid body model of the complex in (D). (**H**) Models of C3b, iC3b, and the CR3:iC3b complex on an activator surface with coloring as in (D)–(F). C3b is deposited on the surface and cleaved by FI into iC3b. The degraded CUB domain in iC3b extends releasing the C3c moiety of iC3b from the TE domain. Upon CR3 recognition, the CUB domain reorganizes substantially.

allow us to define a unique position of the C3c fragment relative to the rest of the complex as rather different C3c orientations are observed in the three clusters of models (Fig. 5D–F, Supplemental Fig. 4D–F).

The DAMMIF program was used to generate 40 ab initio models from the CR3:iC3b scattering curve. The models were subsequently clustered using DAMCLUST, which gave one major cluster containing 32 models. The models were aligned and averaged, which resulted in a flat and extended ab initio envelope, with similar dimensions to the rigid body models (Fig. 5G). Taken together, our SAXS data support a model in which upon CR3 recognition, the C3c and TE domain moieties of iC3b are brought closer to one another because of recognition by CR3 of regions outside the TE domain. This results in a compact receptor–ligand complex, which

upon extrapolation to an opsonized cell recognized by CR3, predicts the C3c moiety of iC3b to be overall much closer to the activator rather than extended away from the surface as predicted for C3b (Fig. 5H).

Discussion

Our prior crystal structure and biophysical experiments of the α_MI–C3d complex defined the core of the iC3b–CR3 interaction centered on the coordination of the divalent cation in the α_MI metal ion–dependent binding site by an aspartate from the iC3b TE domain. It was further demonstrated that C3d and C3dg bound the α_M I-domain with an affinity resembling that of the iC3b–α_M I-domain interaction (30, 56). This C3d(g) –CR3 interaction appears to have physiological relevance because C3dg-mediated erythrophagocytosis may occur in individuals suffering from paroxysmal nocturnal hemoglobinuria (56). However, other regions in CR3 beside the α_M I-domain must contribute to iC3b binding because its deletion leaves residual iC3b affinity in CR3 (34). We detected a weak Mg^{2+}-independent interaction, but whether this only reflects iC3b interactions with regions in the CR3 headpiece outside the α_M I-domain remains open. Both the α_M β-propeller and the β_2 I-like domain have been implicated in interaction with iC3b (34, 36, 57, 58), and on the iC3b side, mutations in the iC3b Nt-α' region associating with the MG7 domain weaken the iC3b–CR3 interaction (35). All these prior lines of evidence are consistent with a higher affinity of the CR3 headpiece for iC3b as compared with C3dg.

Prior studies have disagreed upon the affinity of CR3 for iC3b and have been limited by a number of factors, including activation state of the receptor, purity of the protein preparations, and degree of oligomerization of the iC3b preparations (31, 32). We now quantitate the binding using highly pure and well-characterized proteins and show that the CR3 headpiece recognized iC3b with a K_d of 30 nM in Mg^{2+}/Ca^{2+}. This represents a 17-fold higher affinity than the 515 nM observed for the CR3–C3d interaction in Mg^{2+}/Ca^{2+} and is, to our knowledge, the highest monovalent affinity measured between C3b, iC3b, C3dg, and their five complement receptors. In the presence of Mn^{2+}, we observe a K_d of 6 nM, confirming the model for how Mn^{2+} regulates the ligand affinity of integrin receptors (59). Although the difference in ΔG for dissociation constants of 30 and 515 nM only corresponds to 7 kJ/mol because of multiple complexes formed between a phagocyte and an iC3b opsonized activator, a strong effect is predicted to result in vivo. Hence, the much more efficient phagocytosis of iC3b-tagged objects compared with those tagged by C3dg can be rationalized. Importantly, it is only the combination of the CR3 headpiece and iC3b that results in this high-affinity interaction as both the CR3–C3d (this study) and the α_MI-iC3b interactions (30) have K_d values of 500–600 nM. Thus, omission of the CUB and C3c moities of iC3b or of the βI and β-propeller moieties of CR3 result in lower affinities, agreeing with our finding that these moieties come close to one another in iC3b–CR3 complexes.

To probe the functional similarity between our recombinant CR3 headpiece and cell membrane–expressed CR3 with respect to binding iC3b, a solution-based quantitative assay was established. CR3/K562 cells, or parental wild-type K562 cell as controls, were incubated with CR3-activating agents and fluorophore-conjugated iC3b for sufficient time to reach equilibrium. The binding of iC3b* to CR3 followed closely a Langmuir–Hill isotherm and enabled a robust estimation of the apparent K_d to ∼50 nM. This is in close agreement with the values for CR3 headpiece binding to iC3b determined by SPR, especially for conditions containing Mg^{2+}/Ca^{2+}. Hence, the binding of iC3b to cell-bound CR3, and the soluble CR3 headpiece appears to be quantitatively similar. The equilibrium data obtained with the CR3-expressing cells also permits estimation of the Hill coefficient, which was in the range of 1.7–2.6, depending on the mode of CR3 activation. As noted elsewhere (60), only under specific conditions of marked positive cooperativity does the coefficient enumerate binding stoichiometry. A better understanding embodies the coefficient as a correlate of the extent of cooperativity in ligand interactions, including those reflecting structural rearrangements to strengthen binding (60). We speculate that the positive cooperativity suggested by the Hill coefficient may receive a contribution from rearrangements occurring in the membrane-bound CR3 as part of the conformational outside-in signal induced by ligand binding in integrin receptors.

We also observed that it was possible to use the CR3 headpiece as a competitive inhibitor of cellular CR3 binding to iC3b. IC_{50} values were at 200–250 nM or 4–5-fold higher than expected from a simple 1:1 binding reaction between the CR3 headpiece and iC3b. Both we and others (2) observed that the CR3 headpiece forms dimers in solution, which are unable to interact with iC3b. Alternatively, the CR3 headpiece may weakly interact with the K562 cells in a manner competing with binding of iC3b*. Both effects may explain why the IC_{50} values are significantly higher than the dissociation constant determined with SPR for the iC3b–CR3 headpiece interaction with the pure components. Nevertheless, the strong ability to compete for iC3b binding again points to the CR3 headpiece as an adequate soluble model for intact CR3 in the cell membrane.

Our rigid body models of the CR3:iC3b complex suggest that the C3c moiety of iC3b is in close proximity to CR3. A comparison with our models of unbound iC3b suggest that the TE domain is brought closer to the C3c moiety upon CR3 binding. The heterogeneity in our SAXS models with respect to the location of the C3c moiety of iC3b relative to CR3 may reflect the in vivo situation. Alternatively, the limited information content present in the underlying SAXS data can give rise to rigid body models that, from a structural point of view, are quite different but fit the data equally well. The system is also challenging for SAXS rigid body refinement because of the difficulty of modeling the remnants of the CUB domain. Our refinement strategy was also conservative, using only four rigid bodies to describe a 300 kDa complex with a D_{max} of 26 nm. Despite these limitations, our SAXS models are overall compatible with an ensemble of CR3–iC3b orientations seen in a recent nsEM study (2), except that those complexes showed more separation between the end of the C3c MG-ring bearing the C345c domain and the CR3 β_I–β-propeller interface. The authors in (2) suggested a second, three-dimensional contact formed between the integrin and iC3b that was less stable than the α_MI-TE domain contact and was susceptible to disruption when iC3b–CR3 complexes adsorbed to the grid and became largely planar. These results are consistent with a lack of coplanarity of the MG-ring of C3c and the integrin headpiece in our rigid body models. We have also been unable to observe compact iC3b–CR3 complex particles using nsEM grids despite extensive efforts and the use of gradient fixation (61). Furthermore, we consistently observe aggregation of the iC3b–CR3 headpiece complex and its components on cryo-EM grids, and comprehensive screening have not offered any crystals of the complex. These unsuccessful efforts agree with an iC3b–CR3 complex that, although compact, adopts multiple conformations. Possibly only cryotomography studies of an iC3b-tagged object recognized by a CR3-expressing cell is able to provide a more detailed structural model for this pivotal receptor–ligand interaction underlying phagocytosis of complement-opsonized activators.

The structural arrangement of iC3b has been somewhat controversial, with prior SAXS and nsEM studies disagreeing both within and between methods (2–4, 62, 63). In most EM-based studies, the

TE domain was observed to be flexibly attached to the C3c moiety (2–4, 63). However, in one EM study, the TE domain was found stably associated with the C345c domain (62). This study also presented SAXS data with significantly lower values of D_{max} and R_g than those observed by us and others (3, 62). Our data are more in line with other EM-based models of iC3b, in which the TE domain is loosely associated with the C3c moiety through an extended CUB domain (2–4, 63). Hydrogen deuterium exchange data provided evidence that the degraded CUB domain is devoid of secondary structure and therefore suggested to be highly disordered (5). Nevertheless, in our rigid body modeling of iC3b, we observe a nonrandom and preferred location of the CUB and TE domains, which is counterintuitive if the CUB domain indeed is disordered. Further experiments are required to settle whether the TE domain indeed has a preferred location in iC3b or an inherent limitation in our modeling approach gives rise to the observed tight clustering of iC3b models.

Inhibition of specific CR3–ligand interactions has been investigated for decades but is complicated by the plethora of structurally diverse CR3 ligands reported. Multiple CR3 function blocking Abs are known (64–66), and small molecules known as leukadherins binding CR3 and suppressing outside-in signaling upon ligand binding reduce inflammation and suppress tumor growth in animal models of cancer (67, 68). Recent developments in neurobiology are likely to fuel the interest for an iC3b-specific CR3 inhibitor. During development, the activation of the classical pathway of complement on weakly signaling synapses leads to iC3b deposition and recognition by CR3-expressing microglia, which phagocytize the iC3b-opsonized synapses (8, 9, 69). Very recently, microglia CR3 was shown to support complement-dependent synapse elimination by microglia as a mechanism underlying the forgetting of remote memories (70). However, the same pathway that ensures correct development and removal of remote memories by pruning excess synapses is linked to Alzheimer disease (13), frontotemporal dementia (69), and spinal muscular atrophy (71). Our demonstration of a stable and compact complex between iC3b and the CR3 headpiece with a dissociation constant in the low nanomolar range offers hope for the development of molecules capable of specifically interfering with the iC3b:CR3 interaction while preserving the ability of CR3 to recognize its many other noncomplement ligands. In particular, the binding site for the CR3 α_M I-domain in ICAM-1, another CR3 ligand of major physiological relevance, has been mapped to its third Ig domain, and there are currently no indications of contributions from other parts of ICAM-1 (72). Hence, therapeutic molecules specifically disrupting iC3b–CR3 interactions taking place outside of the core C3d–α_M I-domain contact zone are likely to leave CR3 recognition of ICAM-1 and possibly many other CR3 ligands unaffected. Our combined functional and structural studies presented in this study demonstrate that the CR3 headpiece represents a valuable proxy for cell-bound CR3 that is suitable as a target for the development of such selective therapeutic molecules.

Acknowledgments

We thank the staff at the P12 beamline at PETRA III for help during data collection and Lise Arleth and Jan Skov Pedersen for discussions on correction of SAXS data. We acknowledge Christine Schar for assistance with SPR and Karen Margrethe Nielsen and Bettina W. Grumsen for excellent technical assistance with cell culture work and flow cytometry. We acknowledge Josefine Lorentzen for help with BLI data acquisition.

Disclosures

The authors have no financial conflicts of interest.

References

1. Zipfel, P. F., and C. Skerka. 2009. Complement regulators and inhibitory proteins. *Nat. Rev. Immunol.* 9: 729–740.
2. Xu, S., J. Wang, J. H. Wang, and T. A. Springer. 2017. Distinct recognition of complement iC3b by integrins $\alpha_X\beta_2$ and $\alpha_M\beta_2$. *Proc. Natl. Acad. Sci. USA.* 114: 3403–3408.
3. Xue, X., J. Wu, D. Ricklin, F. Forneris, P. Di Crescenzio, C. Q. Schmidt, J. Granneman, T. H. Sharp, J. D. Lambris, and P. Gros. 2017. Regulator-dependent mechanisms of C3b processing by factor I allow differentiation of immune responses. *Nat. Struct. Mol. Biol.* 24: 643–651.
4. Nishida, N., T. Walz, and T. A. Springer. 2006. Structural transitions of complement component C3 and its activation products. *Proc. Natl. Acad. Sci. USA.* 103: 19737–19742.
5. Papanastasiou, M., S. Koutsogiannaki, Y. Sarigiannis, B. V. Geisbrecht, D. Ricklin, and J. D. Lambris. 2017. Structural implications for the formation and function of the complement effector protein iC3b. *J. Immunol.* 198: 3326–3335.
6. Vorup-Jensen, T., and R. K. Jensen. 2018. Structural immunology of complement receptors 3 and 4. *Front. Immunol.* 9: 2716.
7. Erdei, A., S. Lukácsi, B. Mácsik-Valent, Z. Nagy-Baló, I. Kurucz, and Z. Bajtay. 2019. Non-identical twins: different faces of CR3 and CR4 in myeloid and lymphoid cells of mice and men. *Semin. Cell Dev. Biol.* 85: 110–121.
8. Stevens, B., N. J. Allen, L. E. Vazquez, G. R. Howell, K. S. Christopherson, N. Nouri, K. D. Micheva, A. K. Mehalow, A. D. Huberman, B. Stafford, et al. 2007. The classical complement cascade mediates CNS synapse elimination. *Cell.* 131: 1164–1178.
9. Schafer, D. P., E. K. Lehrman, A. G. Kautzman, R. Koyama, A. R. Mardinly, R. Yamasaki, R. M. Ransohoff, M. E. Greenberg, B. A. Barres, and B. Stevens. 2012. Microglia sculpt postnatal neural circuits in an activity and complement-dependent manner. *Neuron.* 74: 691–705.
10. Wakselman, S., C. Béchade, A. Roumier, D. Bernard, A. Triller, and A. Bessis. 2008. Developmental neuronal death in hippocampus requires the microglial CD11b integrin and DAP12 immunoreceptor. *J. Neurosci.* 28: 8138–8143.
11. Jiang, L., S. H. Chen, C. H. Chu, S. J. Wang, E. Oyarzabal, B. Wilson, V. Sanders, K. Xie, Q. Wang, and J. S. Hong. 2015. A novel role of microglial NADPH oxidase in mediating extra-synaptic function of norepinephrine in regulating brain immune homeostasis. *Glia.* 63: 1057–1072.
12. Kadioglu, A., K. De Filippo, M. Bangert, V. E. Fernandes, L. Richards, K. Jones, P. W. Andrew, and N. Hogg. 2011. The integrins Mac-1 and alpha4beta1 perform crucial roles in neutrophil and T cell recruitment to lungs during *Streptococcus pneumoniae* infection. *J. Immunol.* 186: 5907–5915.
13. Hong, S., V. F. Beja-Glasser, B. M. Nfonoyim, A. Frouin, S. Li, S. Ramakrishnan, K. M. Merry, Q. Shi, A. Rosenthal, B. A. Barres, et al. 2016. Complement and microglia mediate early synapse loss in Alzheimer mouse models. *Science.* 352: 712–716.
14. Heesters, B. A., C. E. van der Poel, A. Das, and M. C. Carroll. 2016. Antigen presentation to B cells. *Trends Immunol.* 37: 844–854.
15. Li, J., and T. A. Springer. 2018. Energy landscape differences among integrins establish the framework for understanding activation. *J. Cell Biol.* 217: 397–412.
16. Luo, B. H., and T. A. Springer. 2006. Integrin structures and conformational signaling. *Curr. Opin. Cell Biol.* 18: 579–586.
17. Springer, T. A., and M. L. Dustin. 2012. Integrin inside-out signaling and the immunological synapse. *Curr. Opin. Cell Biol.* 24: 107–115.
18. Li, J., and T. A. Springer. 2017. Integrin extension enables ultrasensitive regulation by cytoskeletal force. *Proc. Natl. Acad. Sci. USA.* 114: 4685–4690.
19. Diamond, M. S., J. Garcia-Aguilar, J. K. Bickford, A. L. Corbi, and T. A. Springer. 1993. The I domain is a major recognition site on the leukocyte integrin Mac-1 (CD11b/CD18) for four distinct adhesion ligands. *J. Cell Biol.* 120: 1031–1043.
20. Chavakis, T., A. Bierhaus, N. Al-Fakhri, D. Schneider, S. Witte, T. Linn, M. Nagashima, J. Morser, B. Arnold, K. T. Preissner, and P. P. Nawroth. 2003. The pattern recognition receptor (RAGE) is a counterreceptor for leukocyte integrins: a novel pathway for inflammatory cell recruitment. *J. Exp. Med.* 198: 1507–1515.
21. Lishko, V. K., V. P. Yakubenko, T. P. Ugarova, and N. P. Podolnikova. 2018. Leukocyte integrin Mac-1 (CD11b/CD18, $\alpha_M\beta_2$, CR3) acts as a functional receptor for platelet factor 4. *J. Biol. Chem.* 293: 6869–6882.
22. Liu, Y. S., L. F. Wang, X. S. Cheng, Y. N. Huo, X. M. Ouyang, L. Y. Liang, Y. Lin, J. F. Wu, J. L. Ren, and B. Guleng. 2019. The pattern-recognition molecule mindin binds integrin Mac-1 to promote macrophage phagocytosis via Syk activation and NF-κB p65 translocation. *J. Cell. Mol. Med.* 23: 3402–3416.
23. Morgan, J., M. Saleem, R. Ng, C. Armstrong, S. S. Wong, S. G. Caulton, A. Fickling, H. E. L. Williams, A. D. Munday, J. A. López, et al. 2019. Structural basis of the leukocyte integrin Mac-1 I-domain interactions with the platelet glycoprotein Ib. *Blood Adv.* 3: 1450–1459.
24. Saggu, G., K. Okubo, Y. Chen, R. Vattepu, N. Tsuboi, F. Rosetti, X. Cullere, N. Washburn, S. Tahir, A. M. Rosado, et al. 2018. Cis interaction between sialylated FcγRIIA and the αI-domain of Mac-1 limits antibody-mediated neutrophil recruitment. *Nat. Commun.* 9: 5058.
25. Wolf, D., J. D. Hohmann, A. Wiedemann, K. Bledzka, H. Blankenbach, T. Marchini, K. Gutte, K. Zeschky, N. Bassler, N. Hoppe, et al. 2011. Binding of CD40L to Mac-1's I-domain involves the EQLKKSKTL motif and mediates leukocyte recruitment and atherosclerosis–but does not affect immunity and thrombosis in mice. *Circ. Res.* 109: 1269–1279.
26. Zhang, X., G. Bajic, G. R. Andersen, S. H. Christiansen, and T. Vorup-Jensen. 2016. The cationic peptide LL-37 binds Mac-1 (CD11b/CD18) with a low dissociation rate and promotes phagocytosis. *Biochim. Biophys. Acta.* 1864: 471–478.

27. DuMont, A. L., P. Yoong, C. J. Day, F. Alonzo III, W. H. McDonald, M. P. Jennings, and V. J. Torres. 2013. *Staphylococcus aureus* LukAB cytotoxin kills human neutrophils by targeting the CD11b subunit of the integrin Mac-1. *Proc. Natl. Acad. Sci. USA.* 110: 10794–10799.
28. Ranganathan, S., C. Cao, J. Catania, M. Migliorini, L. Zhang, and D. K. Strickland. 2011. Molecular basis for the interaction of low density lipoprotein receptor-related protein 1 (LRP1) with integrin alphaMbeta2: identification of binding sites within alphaMbeta2 for LRP1. *J. Biol. Chem.* 286: 30535–30541.
29. Vorup-Jensen, T. 2012. On the roles of polyvalent binding in immune recognition: perspectives in the nanoscience of immunology and the immune response to nanomedicines. *Adv. Drug Deliv. Rev.* 64: 1759–1781.
30. Bajic, G., L. Yatime, R. B. Sim, T. Vorup-Jensen, and G. R. Andersen. 2013. Structural insight on the recognition of surface-bound opsonins by the integrin I domain of complement receptor 3. *Proc. Natl. Acad. Sci. USA.* 110: 16426–16431.
31. Cai, T. Q., and S. D. Wright. 1995. Energetics of leukocyte integrin activation. *J. Biol. Chem.* 270: 14358–14365.
32. Gordon, D. L., G. M. Johnson, and M. K. Hostetter. 1987. Characteristics of iC3b binding to human polymorphonuclear leucocytes. *Immunology.* 60: 553–558.
33. Gaither, T. A., I. Vargas, S. Inada, and M. M. Frank. 1987. The complement fragment C3d facilitates phagocytosis by monocytes. *Immunology.* 62: 405–411.
34. Yalamanchili, P., C. Lu, C. Oxvig, and T. A. Springer. 2000. Folding and function of I domain-deleted Mac-1 and lymphocyte function-associated antigen-1. *J. Biol. Chem.* 275: 21877–21882.
35. Taniguchi-Sidle, A., and D. E. Isenman. 1994. Interactions of human complement component C3 with factor B and with complement receptors type 1 (CR1, CD35) and type 3 (CR3, CD11b/CD18) involve an acidic sequence at the N-terminus of C3 alpha'-chain. *J. Immunol.* 153: 5285–5302.
36. Li, Y., and L. Zhang. 2003. The fourth blade within the beta-propeller is involved specifically in C3bi recognition by integrin alpha M beta 2. *J. Biol. Chem.* 278: 34395–34402.
37. Suloway, C., J. Pulokas, D. Fellmann, A. Cheng, F. Guerra, J. Quispe, S. Stagg, C. S. Potter, and B. Carragher. 2005. Automated molecular microscopy: the new Leginon system. *J. Struct. Biol.* 151: 41–60.
38. Voss, N. R., C. K. Yoshioka, M. Radermacher, C. S. Potter, and B. Carragher. 2009. DoG Picker and TiltPicker: software tools to facilitate particle selection in single particle electron microscopy. *J. Struct. Biol.* 166: 205–213.
39. Lander, G. C., S. M. Stagg, N. R. Voss, A. Cheng, D. Fellmann, J. Pulokas, C. Yoshioka, C. Irving, A. Mulder, P. W. Lau, et al. 2009. Appion: an integrated, database-driven pipeline to facilitate EM image processing. *J. Struct. Biol.* 166: 95–102.
40. Scheres, S. H. 2012. RELION: implementation of a Bayesian approach to cryo-EM structure determination. *J. Struct. Biol.* 180: 519–530.
41. Jensen, R. K., R. Pihl, T. A. F. Gadeberg, J. K. Jensen, K. R. Andersen, S. Thiel, N. S. Laursen, and G. R. Andersen. 2018. A potent complement factor C3-specific nanobody inhibiting multiple functions in the alternative pathway of human and murine complement. *J. Biol. Chem.* 293: 6269–6281.
42. Pedersen, D. V., L. Roumenina, R. K. Jensen, T. A. Gadeberg, C. Marinozzi, C. Picard, T. Rybkine, S. Thiel, U. B. Sørensen, C. Stover, et al. 2017. Functional and structural insight into properdin control of complement alternative pathway amplification. *EMBO J.* 36: 1084–1099.
43. Li, J., Y. Su, W. Xia, Y. Qin, M. J. Humphries, D. Vestweber, C. Cabañas, C. Lu, and T. A. Springer. 2017. Conformational equilibria and intrinsic affinities define integrin activation. *EMBO J.* 36: 629–645.
44. Schack, L., R. Stapulionis, B. Christensen, E. Kofod-Olsen, U. B. Skov Sørensen, T. Vorup-Jensen, E. S. Sørensen, and P. Höllsberg. 2009. Osteopontin enhances phagocytosis through a novel osteopontin receptor, the alphaXbeta2 integrin. *J. Immunol.* 182: 6943–6950.
45. Robinson, M. K., D. Andrew, H. Rosen, D. Brown, S. Ortlepp, P. Stephens, and E. C. Butcher. 1992. Antibody against the Leu-CAM beta-chain (CD18) promotes both LFA-1- and CR3-dependent adhesion events. *J. Immunol.* 148: 1080–1085.
46. Jarmoskaite, I., I. AlSadhan, P. P. Vaidyanathan, and D. Herschlag. 2020. How to measure and evaluate binding affinities. *Elife.* 9: e57264.
47. Blanchet, C. E., A. Spilotros, F. Schwemmer, M. A. Graewert, A. Kikhney, C. M. Jeffries, D. Franke, D. Mark, R. Zengerle, F. Cipriani, et al. 2015. Versatile sample environments and automation for biological solution X-ray scattering experiments at the P12 beamline (PETRA III, DESY). *J. Appl. Cryst.* 48: 431–443.
48. Graewert, M. A., D. Franke, C. M. Jeffries, C. E. Blanchet, D. Ruskule, K. Kuhle, A. Flieger, B. Schäfer, B. Tartsch, R. Meijers, and D. I. Svergun. 2015. Automated pipeline for purification, biophysical and x-ray analysis of biomacromolecular solutions. *Sci. Rep.* 5: 10734.
49. Panjkovich, A., and D. I. Svergun. 2018. CHROMIXS: automatic and interactive analysis of chromatography-coupled small-angle X-ray scattering data. *Bioinformatics.* 34: 1944–1946.
50. Petoukhov, M. V., D. Franke, A. V. Shkumatov, G. Tria, A. G. Kikhney, M. Gajda, C. Gorba, H. D. Mertens, P. V. Konarev, and D. I. Svergun. 2012. New developments in the *ATSAS* program package for small-angle scattering data analysis. *J. Appl. Cryst.* 45: 342–350.
51. Franke, D., A. G. Kikhney, and D. I. Svergun. 2012. Automated acquisition and analysis of small angle X-ray scattering data. *Nucl Instrum Meth A.* 689: 52–59.
52. Svergun, D. I. 1992. Determination of the regularization parameter in indirect-transform methods using perceptual criteria. *J. Appl. Cryst.* 25: 495–503.
53. Kozin, M. B., and D. I. Svergun. 2001. Automated matching of high- and low-resolution structural models. *J. Appl. Cryst.* 34: 33–41.
54. Xiao, T., J. Takagi, B. S. Coller, J. H. Wang, and T. A. Springer. 2004. Structural basis for allostery in integrins and binding to fibrinogen-mimetic therapeutics. *Nature.* 432: 59–67.
55. Rodriguez, E., R. Nan, K. Li, J. Gor, and S. J. Perkins. 2015. A revised mechanism for the activation of complement C3 to C3b: a molecular explanation of a disease-associated polymorphism. *J. Biol. Chem.* 290: 2334–2350.
56. Lin, Z., C. Q. Schmidt, S. Koutsogiannaki, P. Ricci, A. M. Risitano, J. D. Lambris, and D. Ricklin. 2015. Complement C3dg-mediated erythrophagocytosis: implications for paroxysmal nocturnal hemoglobinuria. *Blood.* 126: 891–894.
57. MacPherson, M., H. S. Lek, A. Prescott, and S. C. Fagerholm. 2011. A systemic lupus erythematosus-associated R77H substitution in the CD11b chain of the Mac-1 integrin compromises leukocyte adhesion and phagocytosis. *J. Biol. Chem.* 286: 17303–17310.
58. Xiong, Y.-M., T. A. Haas, and L. Zhang. 2002. Identification of functional segments within the beta2I-domain of integrin alphaMbeta2. *J. Biol. Chem.* 277: 46639–46644.
59. Chen, J., A. Salas, and T. A. Springer. 2003. Bistable regulation of integrin adhesiveness by a bipolar metal ion cluster. *Nat. Struct. Biol.* 10: 995–1001.
60. Weiss, J. N. 1997. The Hill equation revisited: uses and misuses. *FASEB J.* 11: 835–841.
61. Stark, H. 2010. GraFix: stabilization of fragile macromolecular complexes for single particle cryo-EM. *Methods Enzymol.* 481: 109–126.
62. Alcorlo, M., R. Martínez-Barricarte, F. J. Fernández, C. Rodríguez-Gallego, A. Round, M. C. Vega, C. L. Harris, S. R. de Cordoba, and O. Llorca. 2011. Unique structure of iC3b resolved at a resolution of 24 Å by 3D-electron microscopy. [Published erratum appears in 2011 *Proc. Natl. Acad. Sci. USA.* 108: 16481.] *Proc. Natl. Acad. Sci. USA.* 108: 13236–13240.
63. Chen, X., Y. Yu, L. Z. Mi, T. Walz, and T. A. Springer. 2012. Molecular basis for complement recognition by integrin αXβ2. *Proc. Natl. Acad. Sci. USA.* 109: 4586–4591.
64. Oxvig, C., C. Lu, and T. A. Springer. 1999. Conformational changes in tertiary structure near the ligand binding site of an integrin I domain. *Proc. Natl. Acad. Sci. USA.* 96: 2215–2220.
65. Mahalingam, B., K. Ajroud, J. L. Alonso, S. Anand, B. D. Adair, A. L. Horenstein, F. Malavasi, J. P. Xiong, and M. A. Arnaout. 2011. Stable coordination of the inhibitory Ca2+ ion at the metal ion-dependent adhesion site in integrin CD11b/CD18 by an antibody-derived ligand aspartate: implications for integrin regulation and structure-based drug design. *J. Immunol.* 187: 6393–6401.
66. Wolf, D., N. Anto-Michel, H. Blankenbach, A. Wiedemann, K. Buscher, J. D. Hohmann, B. Lim, M. Bäuml, A. Marki, M. Mauler, et al. 2018. A ligand-specific blockade of the integrin Mac-1 selectively targets pathologic inflammation while maintaining protective host-defense. *Nat. Commun.* 9: 525.
67. Schmid, M. C., S. Q. Khan, M. M. Kaneda, P. Pathria, R. Shepard, T. L. Louis, S. Anand, G. Woo, C. Leem, M. H. Faridi, et al. 2018. Integrin CD11b activation drives anti-tumor innate immunity. *Nat. Commun.* 9: 5379.
68. Maiguel, D., M. H. Faridi, C. Wei, Y. Kuwano, K. M. Balla, D. Hernandez, C. J. Barth, G. Lugo, M. Donnelly, A. Nayer, et al. 2011. Small molecule-mediated activation of the integrin CD11b/CD18 reduces inflammatory disease. *Sci. Signal.* 4: ra57.
69. Lui, H., J. Zhang, S. R. Makinson, M. K. Cahill, K. W. Kelley, H. Y. Huang, Y. Shang, M. C. Oldham, L. H. Martens, F. Gao, et al. 2016. Progranulin Deficiency Promotes Circuit-Specific Synaptic Pruning by Microglia via Complement Activation. *Cell.* 165: 921–935.
70. Wang, C., H. Yue, Z. Hu, Y. Shen, J. Ma, J. Li, X. D. Wang, L. Wang, B. Sun, P. Shi, et al. 2020. Microglia mediate forgetting via complement-dependent synaptic elimination. *Science.* 367: 688–694.
71. Vukojicic, A., N. Delestrée, E. V. Fletcher, J. G. Pagiazitis, S. Sankaranarayanan, T. A. Yednock, B. A. Barres, and G. Z. Mentis. 2019. The classical complement pathway mediates microglia-dependent remodeling of spinal motor circuits during development and in SMA. *Cell Rep.* 29: 3087–3100.e7.
72. Diamond, M. S., D. E. Staunton, S. D. Marlin, and T. A. Springer. 1991. Binding of the integrin Mac-1 (CD11b/CD18) to the third immunoglobulin-like domain of ICAM-1 (CD54) and its regulation by glycosylation. *Cell.* 65: 961–971.